

See discussions, stats, and author profiles for this publication at: <https://www.researchgate.net/publication/287971563>

# Beyond Graphene Foam, a New Form of Three-Dimensional Graphene for Supercapacitor Electrode

Article in *Journal of Materials Chemistry A* · December 2015

DOI: 10.1039/C5TA10031C

CITATIONS

21

READS

165

9 authors, including:



**Lu Zhang**

University of California, Los Angeles

16 PUBLICATIONS 543 CITATIONS

[SEE PROFILE](#)



**Noe Alvarez**

University of Cincinnati

37 PUBLICATIONS 371 CITATIONS

[SEE PROFILE](#)

Some of the authors of this publication are also working on these related projects:



Effects of laser cutting on the structural and mechanical properties of carbon nanotube assemblages [View project](#)



Targeted mass spectrometry [View project](#)



Cite this: *J. Mater. Chem. A*, 2016, 4, 1876

## Beyond graphene foam, a new form of three-dimensional graphene for supercapacitor electrodes†

Lu Zhang,<sup>a</sup> Derek DeArmond,<sup>ab</sup> Noe T. Alvarez,<sup>b</sup> Daoli Zhao,<sup>c</sup> Tingting Wang,<sup>c</sup> Guangfeng Hou,<sup>a</sup> Rachit Malik,<sup>a</sup> William R. Heineman<sup>c</sup> and Vesselin Shanov<sup>\*ab</sup>

Graphene foam (GF) is a three-dimensional (3D) graphene structure that has been intensively studied as an electrode material for energy storage applications. The porous structure and seamlessly connected graphene flakes make GF a promising electrode material for supercapacitors and batteries. However, the electrical conductivity of GF is still unsatisfactory due to the lack of macropore size ( $\sim 300\ \mu\text{m}$ ) control that hinders its applications. Previously we reported a new seamless 3D graphene structure – graphene pellets (GPs) – with well-controlled mesopore size ( $\sim 2\ \text{nm}$ ), high electrical conductivity ( $148\ \text{S cm}^{-1}$ ) and good electromechanical properties that differ substantially from the known GF. Here we demonstrate that the obtained 3D graphene structure is an ideal scaffold electrode for pseudocapacitive materials and redox additive electrolyte systems. For example, after electrochemical coating with  $\text{MnO}_2$ , the GP/ $\text{MnO}_2$  electrode showed specific and volumetric capacitance up to  $395\ \text{F g}^{-1}$  and  $230\ \text{F cm}^{-3}$  at  $1\ \text{A g}^{-1}$ , respectively. When combined with a hydroquinone and benzoquinone redox additive electrolyte, the GPs showed a specific capacitance of  $7813\ \text{F g}^{-1}$  at  $10\ \text{A g}^{-1}$ . Moreover, when the GP/ $\text{MnO}_2$  electrode was assembled with a GP/polypyrrole electrode, the obtained full cell showed good electrochemical performance with a maximum energy density of  $26.7\ \text{W h kg}^{-1}$  and a maximum power density of  $32.7\ \text{kW kg}^{-1}$ , and a reasonable cycle life for practical application. The ease in material processing combined with the excellent electrical and electromechanical properties makes GPs promising for a variety of energy storage applications.

Received 9th December 2015  
Accepted 19th December 2015

DOI: 10.1039/c5ta10031c

www.rsc.org/MaterialsA

## 1. Introduction

The seamless three-dimensional (3D) graphene structure known as graphene foam (GF), has attracted attention due to partly inheriting the properties of two dimensional (2D) graphene into its 3D structure.<sup>1</sup> GF morphology ensures fast electron transfer on the 3D graphene skeleton and its porous structure contributes to a high specific surface area of this material. Therefore, since reported in 2011, GF has been intensively investigated for application in energy storage due to its attractive properties, as described below.<sup>2–11</sup> Dong *et al.* reported a GF/ $\text{MnO}_2$  composite prepared from  $\text{KMnO}_4$  with a specific capacitance of  $560\ \text{F g}^{-1}$  at  $0.2\ \text{A g}^{-1}$  in  $1.0\ \text{M Na}_2\text{SO}_4$ .<sup>5</sup> Cao *et al.* have introduced GF with NiO coating and achieved a specific capacitance of  $816\ \text{F g}^{-1}$  at  $5\ \text{mV s}^{-1}$  in  $3\ \text{M KOH}$ .<sup>7</sup> GF

was also employed as an electrode for redox additive electrolyte systems. Luo *et al.* tested a GF/Ni foam/ $\text{Co}(\text{OH})_2$  composite in  $0.08\ \text{M K}_3\text{Fe}(\text{CN})_6/1\ \text{M KOH}$  electrolyte and obtained a specific capacitance of  $7514\ \text{F g}^{-1}$  at  $16\ \text{A g}^{-1}$ . In this case only the mass of  $\text{Co}(\text{OH})_2$  was used for capacitance calculation.<sup>8</sup>

Despite the unique structure of GF that contributes to a fast electron transfer on the graphene skeleton, this material exhibits a poor electrical conductivity of  $\sim 1\ \text{S cm}^{-1}$ . As a consequence, the electrical performance of pseudocapacitive materials such as  $\text{MnO}_2$  and polyaniline used in combination with GF for supercapacitors is not satisfactory. In addition, the relatively slow chemical reactions in battery systems further limit the application of GF in energy storage. The low electrical conductivity of GF is a result of its porous structure. The large macropores help increase the surface area of GF. However, they also contribute a longer electron-transfer pathway that results in low electrical conductivity. Another consequence of the GF morphology is the reduction of its mechanical strength. Because of this mechanical weakness the fabricated electrodes require the additional metal support of the current collectors in a supercapacitor arrangement.

The unfavorable porous structure of GF is inherited from the catalyst used in the chemical vapor deposition (CVD) process,

<sup>a</sup>Department of Mechanical and Materials Engineering, University of Cincinnati, Cincinnati, OH, 45221-0072, USA. E-mail: vesselin.shanov@uc.edu

<sup>b</sup>Department of Biomedical, Chemical and Environmental Engineering, University of Cincinnati, OH, 45221-0012, USA

<sup>c</sup>Department of Chemistry, University of Cincinnati, Cincinnati, OH, 45221-0172, USA

† Electronic supplementary information (ESI) available. See DOI: 10.1039/c5ta10031c

the nickel foam (NF). NF is an expensive material used to synthesize graphene through CVD. Further, GF made from NF yields only 0.4 mg graphene per gram of Ni catalyst. This is a major hurdle that hinders the manufacturing scale up of GF, making it infeasible for the mass production of electrode materials. These drawbacks motivated researchers to work on improving the electrical properties of 3D graphene without increasing the cost of its preparation. Graphene oxide (GO) shows advantages in fabrication considering its low cost thus making it attractive as an electrode material in combination with pseudocapacitive materials such as  $\text{MnO}_2$ .<sup>12–14</sup> However, even after a performed chemical reduction, the residual functional groups such as carboxyl, carbonyl and hydroxyl in GO still decrease its electrical conductivity. Moreover, restacking of graphene sheets during the processing of GO into an electrode decreases the specific surface area (SSA) of the overall electrode structure.<sup>7,15–18</sup> The ability of the GO electrode to compensate the low electron transfer in pseudocapacitive materials and accelerate the chemical processes in battery materials is also challenging and not straightforward.

CVD-made graphene usually exhibits probably the best material quality in terms of low defect concentration and high purity. Considering the drawbacks of NF as a catalyst, other catalyst materials, such as nickel chloride and nickel powder, have been studied recently to synthesize high quality 3D graphene through CVD.<sup>19–22</sup> The challenge using this approach is to successfully consolidate the Ni-containing particles into a sintered body that is capable of acting as an efficient and inexpensive catalyst in the CVD environment yielding 3D graphene with good electrical and mechanical properties.

Previously we reported on making a seamless 3D graphene structure called graphene pellets (GPs) synthesized through CVD by processing inexpensive nickel powders as a catalyst.<sup>19</sup> In this work our efforts have been expanded to demonstrate that the GPs can be successfully employed as an important new platform for fabricating high performance electrode materials for energy storage applications.

## 2. Experimental

### 2.1. Sample preparation

**2.1.1. Fabrication of the graphene pellets (GPs).** Nickel powder (Alfa Aesar) of 2–3  $\mu\text{m}$  average particle size and  $0.68 \text{ m}^2 \text{ g}^{-1}$  in SSA was pelletized into a 6.4 cm diameter pellet using a hydraulic press (Carver, 973214A). The sample described above was heated up to 1000  $^\circ\text{C}$  in a tube furnace (FirstNano, ET1000) under Ar (1000 sccm). Hydrogen (325 sccm) was then introduced for 5 min, to reduce any metal catalyst oxide. Then, 25 sccm of  $\text{CH}_4$  was introduced for 1 minute. The sample was then cooled to room temperature at a rate of  $\sim 100 \text{ }^\circ\text{C min}^{-1}$  under Ar (1000 sccm) and  $\text{H}_2$  (325 sccm). The final 3D graphene structure in the form of a pellet was produced by etching out nickel from the graphene/nickel pellet with 3 M HCl at 80  $^\circ\text{C}$  for 10 h. The obtained GP was washed with DI water to remove the residual acid. Details of the synthesis and procedures for the fabrication of the GPs can be found elsewhere.<sup>19</sup>

**2.1.2. Fabrication of the GP/ $\text{MnO}_2$  electrode.**  $\text{MnO}_2$  was coated on the GP by electrodeposition in the following way. GP was immersed into a plating solution containing 20 mM  $\text{MnSO}_4$  and 100 mM  $\text{Na}_2\text{SO}_4$ , and subjected to 5 min to 40 min deposition under a constant current density of  $2 \text{ mA cm}^{-2}$ . After electrodeposition, the GP was washed with DI water to remove the residual electrolyte, and then dried at 60  $^\circ\text{C}$  for 2 h. The mass of the sample was measured before and after electrodeposition of  $\text{MnO}_2$ , using a microbalance (Sartorius Micro Balance MSE6.6S-000-DF). This enabled the mass ratio of  $\text{MnO}_2$  in the GP/ $\text{MnO}_2$  composite to be calculated.

**2.1.3. Fabrication of the GP/polypyrrole (Ppy) electrode.** The GP/Ppy hybrid electrode was synthesized using an *in situ* polymerization method.<sup>14</sup> Generally, a GP was immersed into a mixture solution of pyrrole (1000  $\mu\text{L}$ , from Sigma-Aldrich), ethanol/DI water/1 M HCl (1 : 1 : 1, v/v/v) and amine *p*-toluenesulfonate (*p*TSNH<sub>4</sub>, dopant, from Byk). Ammonium persulfate (APS,  $(\text{NH}_4)_2\text{S}_2\text{O}_8$ , oxidant, from Fisher Scientific) was then added to the mixture solution and the chemical polymerization was carried out at 0–5  $^\circ\text{C}$  for 30 min. The as-made GP/Ppy sample was then washed with DI water and dried at 50  $^\circ\text{C}$ .

**2.1.4. Assembly of GP/ $\text{MnO}_2$ –GP/Ppy asymmetric ECs.** The asymmetric ECs were fabricated by making the GP/ $\text{MnO}_2$  composite as the positive electrode and the GP/Ppy composite as the negative electrode, and finally assembling both electrodes into a coin cell device. The two electrodes were separated by an aqueous electrolyte (1 M  $\text{Na}_2\text{SO}_4$ ) soaked separator (nitrocellulose film).

### 2.2. Analysis

**2.2.1. Microscopic characterization.** Scanning electron microscopy (SEM) (FEI XL30, 15 kV) and Raman spectroscopy (Renishaw inVia, excited by a 514 nm He–Ne laser with a laser spot size of  $\sim 1 \mu\text{m}^2$ ) were used to characterize the GP. X-ray photoelectron spectroscopy (XPS) data were obtained using a Phi 5300 X-ray Photoelectron Spectrometer with Mg K-alpha X-rays at an accelerating voltage of 15.0 kV ( $h\nu = 1253.6 \text{ eV}$ ) in a chamber maintained at  $10^{-9}$  Torr. The high-resolution scans of C and low-resolution survey scans were analyzed for each sample at two or more separate locations.

**2.2.2. Surface area and pore size measurement.** Brunauer–Emmett–Teller (BET) study of GPs. Nitrogen adsorption–desorption isotherms and Barrett–Joyner–Halenda (BJH) pore size distribution were studied by using a surface characterization analyzer (Micromeritics, 3Flex).

**2.2.3. Electrical and mechanical measurements.** A four-point probe device (Jandel RM3000) was used for electrical measurement of the samples. For conducting the resistance retention test, a two-point probe device was constructed. In this arrangement, copper wires were embedded and connected to GPs with silver paste, which enabled a reliable electrical contact between the copper wires and the GPs. A minimum of three samples were measured to calculate each error bar.

**2.2.4. Electrochemical measurements.** The electrochemical measurements were carried out with a Gamry instrument (Interface 1000) at room temperature using a three-

electrode configuration for the GP and GP/MnO<sub>2</sub> electrodes and two-electrode configuration for asymmetric ECs. In the three-electrode configuration, the freestanding GP and GP/MnO<sub>2</sub> samples served as the working electrode without the use of any metal support. They were combined with a Ag/AgCl reference electrode and a Pt counter electrode in an electrolyte solution of 1 M Na<sub>2</sub>SO<sub>4</sub>. Additives such as 50 mM hydroquinone (HQ) and 50 mM benzoquinone (BQ) were prepared along with 1 M H<sub>2</sub>SO<sub>4</sub> and 30% acetic acid (stabilizer for HQ and BQ) used as the electrolyte. The electrochemical characteristics of ~0.2 mg GPs, ~1 mg GP/MnO<sub>2</sub> composites (total mass of the electrode with both GPs and MnO<sub>2</sub>) and ~5 mg asymmetric ECs (total mass of two electrodes with both GPs and active materials including Ppy and MnO<sub>2</sub>) were evaluated by cyclic voltammetry, galvanostatic charge–discharge and electrochemical impedance spectroscopy measurements over a frequency range from 10<sup>5</sup> to 10<sup>−2</sup> Hz at a sinusoidal voltage amplitude of 10 mV.

The specific capacitance in the three-electrode system was calculated by using the equation  $C = It/(\Delta Vm)$ , and the volumetric capacitance was calculated by a similar expression  $C_v = \rho C$ , where  $I$  is the discharge current,  $t$  is the discharge time,  $\Delta V$  is the operating voltage window,  $m$  is the individual electrode mass (including GPs and active materials), and  $\rho$  is the density of the electrode.<sup>23</sup>

To achieve good capacitance performance of the asymmetric electrochemical supercapacitors (ECs), the mass of the two electrodes was balanced based on the following equation:  $C^- \Delta V^- m^- = C^+ \Delta V^+ m^+$ , where  $C$  is the specific capacitance of a single electrode,  $\Delta V$  is the operating voltage window, and  $m$  is the mass of the electrode.

The energy density ( $E$ ), power density ( $P$ ) and maximal power density ( $P_m$ ) were calculated by the expressions:  $E = C_{\text{cell}}(\Delta V)^2/2$ ,  $P = Et^{-1}$ , and  $P_m = \Delta V^2/4Rm$ , where  $C_{\text{cell}}$  is the cell capacitance calculated by  $C_{\text{cell}} = It/(\Delta Vm)$ ,  $\Delta V$  is the operating voltage window,  $t$  is the discharge time,  $I$  is the discharge current,  $m$  is the total mass of the two electrodes, and  $R$  is the internal resistance calculated from the IR drop of the charge–discharge curve.<sup>24</sup>

### 3. Results and discussion

In order to create a seamless CVD-made 3D graphene structure, a rational design of a 3D structured catalyst is necessary. In our approach, nickel powder of 2 to 3  $\mu\text{m}$  in diameter was pressed to form a nickel pellet and then sintered at 1000 °C under a protective gas flow of argon to prevent oxidation. The pressing and heating steps enable sintering of the Ni powder through necking, which ultimately benefits the formation of a continuous and interconnected three-dimensional graphene structure during the sequential CVD.<sup>19</sup> GPs have a relatively low areal density of 4.5 g m<sup>−2</sup> as shown in Fig. S1.† The process of sintering nickel particles is illustrated in Fig. 1a and b. The rough surface of nickel powder (Fig. 1a) becomes smoother after sintering (Fig. 1b) which leads to the formation of an interconnected structure. Right after sintering the Ni powder in Ar, methane was introduced in the CVD reactor to synthesize graphene. The latter was observed on the surface of the sintered

nickel (Fig. 1c). The freestanding GP was obtained by etching out Ni using HCl acid (Fig. 1d). Fig. 1e shows SEM images of GF and GPs taken under a similar magnification. It is clearly recognizable that GF has a much larger macropore size than GPs. The highly porous structure of GF contributes to a high surface area, but at the same time lowers its electrical conductivity due to the prolonged electron pathway. As will be discussed later on, the electrical conductivity of GF is by 2 orders lower than that of GPs in this work. Moreover, the Ni catalyst used in our study yields 3.0 mg graphene per gram of nickel powder compared to the Ni foam yielding only 0.4 mg per gram of nickel (Table 1).

Fig. 1f displays the typical Raman spectra of a GP. Normally, fewer layers of graphene were observed through the Raman spectra after reducing the methane saturation time during the CVD step. The obtained GPs had robust mechanical properties resulting in good flexibility, as illustrated in Fig. 1g.

The study of SSA, pore size distribution and electrical conductivity is important to realize the performance of a carbon scaffold for pseudocapacitor application. Though the obtained GP has a moderate SSA (~80 m<sup>2</sup> g<sup>−1</sup>), it shows a mesopore (~2 nm) dominated structure (Fig. S2†), which is beneficial in facilitating a quick diffusion of electrolyte ions as suggested by other groups.<sup>25–27</sup> Furthermore, the electrical properties of GPs outperform those of other reported graphene scaffold materials for pseudocapacitor electrode applications<sup>1,12,28,29</sup> as shown in Table 2. The high electrical conductivity (148 S cm<sup>−1</sup>) of GPs is attributed to the good quality of graphene prepared by CVD and improved flake to flake contact compared to graphene samples obtained by wet chemistry methods.<sup>12,29</sup> In addition, due to the compression and the sintering process, the well interconnected nickel grains help to form a seamless 3D graphene structure, which results in a higher electrical conductivity of the samples compared to other CVD-made 3D graphene materials.<sup>1,21,28</sup> The electrical conductivity of the 3D graphene in this work can be controlled by the methane concentration during the CVD process as demonstrated in Fig. 2a. It can be seen here that the electrical conductivity of GPs starts at a relatively low value of 47 S cm<sup>−1</sup> and rises up to 148 S cm<sup>−1</sup> with the increase of methane concentration during CVD. This phenomenon could be attributed to the higher methane concentration causing more graphene to grow on the sintered nickel skeleton, which results in a better-interconnected graphene structure. It is worth mentioning that beyond a critical value of methane concentration, the electrical conductivity decreases. This critical value in our work is 1.9 vol% as observed in Fig. 2a. This is probably due to the inability of the catalyst to absorb methane when the methane concentration exceeds a certain saturation point.<sup>19</sup>

The fast development of wearable devices and related power sources nowadays demands for electrode materials with good mechanical and electrical properties.<sup>30</sup> GPs have beneficial characteristics such as high electrical conductivity, good mechanical robustness, and flexibility. Therefore, they are expected to perform well when incorporated as flexible electrodes in devices integrated with woven and non-woven fabric. We investigated the effect of bending on the electrical resistance of GPs prepared using 1.9 vol% CH<sub>4</sub> with 1 min saturation time

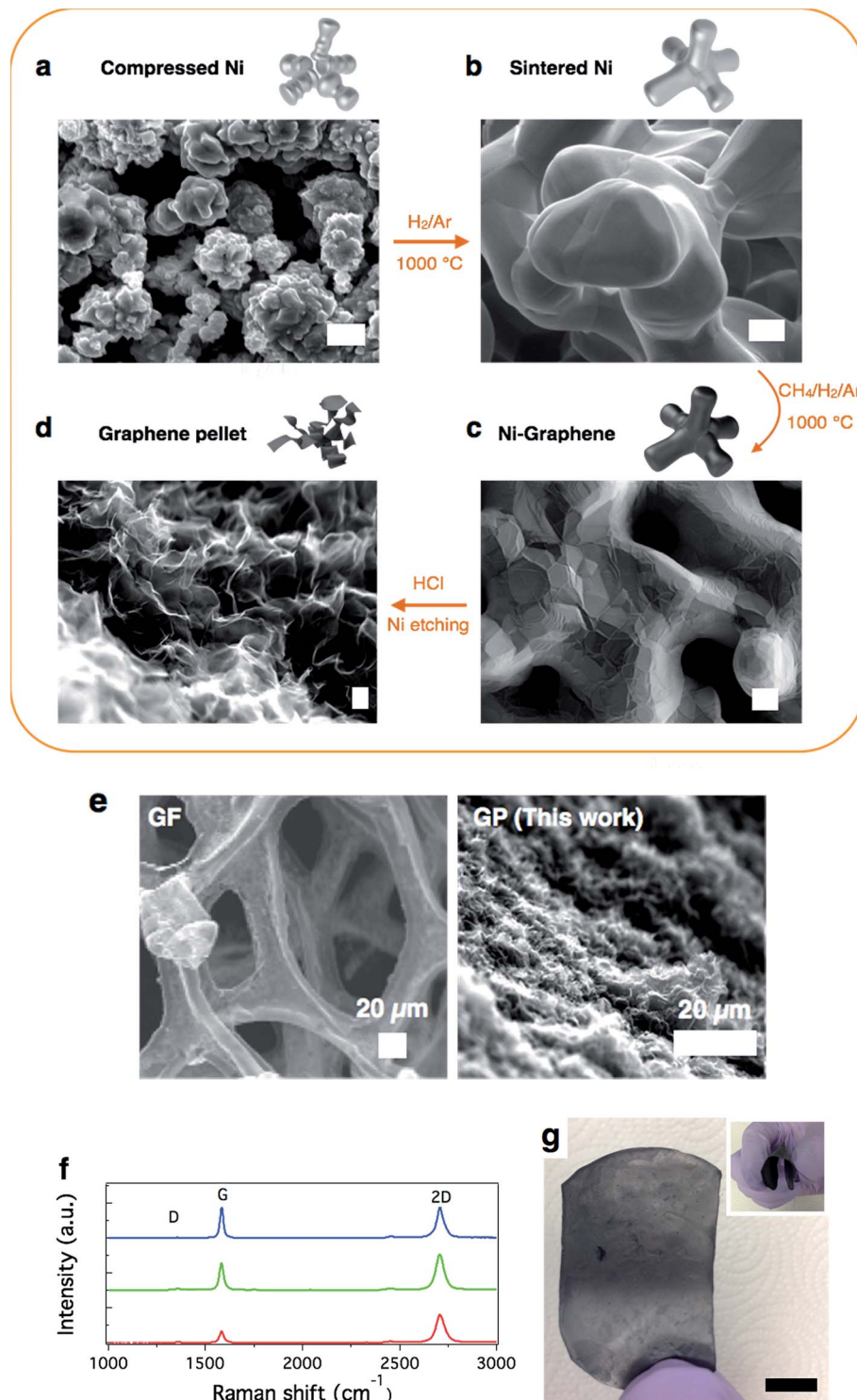


**Fig. 1** (a) Compressed Ni powder with a discrete structure. (b) Sintered Ni powder with a continuous 3D structure. (c) CVD growth of 3D graphene structures on the sintered Ni grains as a 3D scaffold template (Ni-graphene). (d) Free-standing GPs after etching the sintered Ni with heated HCl acid. The scale bars correspond to 3 μm. (e) SEM images for comparison of GF (left) and GPs (right). (f) Typical Raman spectra of a GP prepared with a CH<sub>4</sub> concentration of 1.9 vol%. The three spectra suggest monolayer and multilayer graphene (from bottom to top), respectively, which are examined based on the intensity, shape and position of the G band and 2D band. (g) Photos of GPs. The scale bar corresponds to 1 cm. The inset shows good flexibility of GPs.

during CVD, which reveals the best electrical conductivity among all the prepared samples. The bend and stretch tests were carried out using a 4-point bending device and a high-

precision mechanical system. The electrical resistance revealed a small decrease when bending up to a radius of 1.0 mm and could recover after straightening with a resistance increase of



**Table 1** Comparison of graphene yield and catalyst cost<sup>a</sup> for making GF and GPs

Materials	Graphene yield per gram of catalyst	Catalyst and cost
GF	0.4 mg	Nickel foam (\$0.6 per g)
GPs (this work)	3.0 mg	Nickel powder (\$0.15 per g)

<sup>a</sup> Based on information from Thermo Fisher Scientific Inc.

**Table 2** Electrical conductivity comparison of different graphene scaffolds for EC electrodes

Materials	Electrical conductivity (S cm <sup>-1</sup> )	Reference
Embossed chemically modified graphene	12.04	12
Reduced graphene oxide	5.65	29
Graphene foam	1	1
CNT/graphene foam hybrid film	1.9	28
GPs	148	This work

only 0.21% (Fig. 2b). It is interesting to point out that the resistance of GPs decreased during the bending process, which could be attributed to the compacting effect of 3D GPs during

bending. Fig. 2c shows the cyclic bend and release test of GPs at a very small bend radius of 1.0 mm. The resistance of GPs increases rapidly in the first 10 cycles and becomes stable after 1000 cycles (Fig. 2c inset). There is only 7.3% increase in resistance after 5000 cycles at the tested small bend radius of 1.0 mm. These results illustrate the excellent electromechanical stability of GPs compared with conventional materials used in flexible electronics and other graphene materials such as graphene foam and graphene films.<sup>1,31</sup>

The good electrical and mechanical properties of the 3D graphene pellet make it an excellent candidate for energy storage applications. To explore this opportunity, we chose a typical pseudocapacitive material – MnO<sub>2</sub>, which allowed us to study the synergistic effect between GPs and this metal oxide. A layer of MnO<sub>2</sub> was electrochemically deposited on the surface of GPs by oxidation of Mn<sup>2+</sup> to Mn<sup>4+</sup> in solution, following a procedure described in the literature.<sup>32</sup> Fig. 3a–d show SEM images revealing the morphology of GPs after electrochemical coating with MnO<sub>2</sub> with different mass loadings. The latter was controlled by manipulating the time of electro-deposition, which was varied from 5 min to 40 min. Compared to pristine GPs (Fig. 3a), the deposited GP/MnO<sub>2</sub> (11.4 wt% MnO<sub>2</sub>) in Fig. 3b showed cluster formation of the coating. These clusters transformed into sphere-like structures when the MnO<sub>2</sub> content was increased to 54.5 wt% as shown in Fig. 3c. The inset in the SEM image in Fig. 3c displays the cross-section of GP/MnO<sub>2</sub>

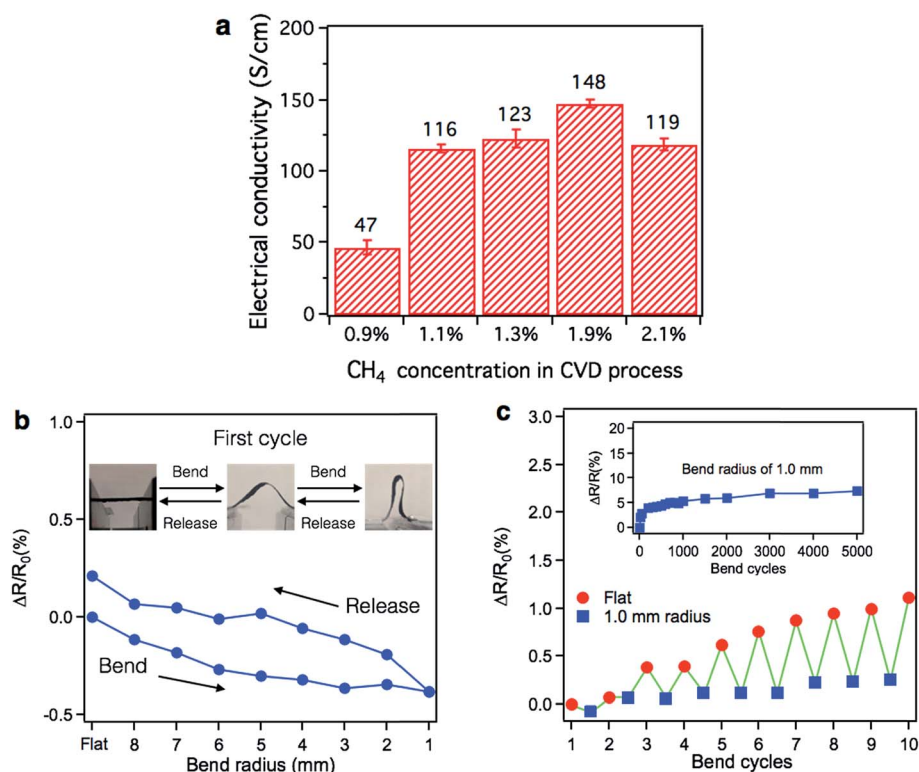


**Fig. 2** (a) Electrical conductivity of the GPs prepared by using different CH<sub>4</sub> concentrations. The error bars represent the standard deviations that were calculated based on 3 tested specimens for each sample. (b) Variation in the electrical resistance of GPs as a function of the bend radius up to 1.0 mm and back to the flat state during a single bend cycle. The inset shows the bend and release steps. (c) Variation in electrical resistance of a composite during bending in cycles with a radius up to 1.0 mm and then back to the flat state. The inset shows the resistance change of GPs as a function of the bend cycles for a bend radius of 1.0 mm.

(54.5 wt%  $\text{MnO}_2$ ), where the embedment of  $\text{MnO}_2$  spheres into the surface of GPs is revealed. This embedment suggests a good contact between  $\text{MnO}_2$  and GPs, which can be attributed to the unique porous surface morphology of GPs. In Fig. 3d showing the morphology of the GP/ $\text{MnO}_2$  (79.6 wt%  $\text{MnO}_2$ ) sample, the spheres of the metal oxide merge into a bulk layer. The inset in the SEM image displays the cross-section view of the coating. Though the thickness of the  $\text{MnO}_2$  layer is relatively large compared to those of other reported studies,<sup>12,33</sup> the good electrical properties of GPs and the intimately integrated  $\text{MnO}_2$  and GPs compensate the low electrical conductivity of  $\text{MnO}_2$ . The calculated areal densities of GP/ $\text{MnO}_2$  composites with 0 wt%, 11.4 wt%, 54.5 wt% and 79.6 wt%  $\text{MnO}_2$  are  $4.5 \text{ g m}^{-2}$ ,  $5.1 \text{ g m}^{-2}$ ,  $9.9 \text{ g m}^{-2}$  and  $22.3 \text{ g m}^{-2}$ , respectively. These data illustrate the ability of GPs to accommodate a high content of  $\text{MnO}_2$ . The formed  $\text{MnO}_2$  thin layer on GPs was further investigated by X-ray photoelectron spectroscopy (XPS). As shown in Fig. 3e, two characteristic peaks of  $\text{Mn } 2p_{1/2}$  and  $\text{Mn } 2p_{3/2}$  at

654.1 and 642.4 eV, respectively, with a binding energy separation of 11.7 eV were observed, which is in good agreement with previous work.<sup>34,35</sup>

The electrochemical performances of GPs and GP/ $\text{MnO}_2$  composites as capacitive electrodes were evaluated using a conventional three-electrode system in an aqueous electrolyte solution of 1 M  $\text{Na}_2\text{SO}_4$ . As shown in Fig. 4a, the cyclic voltammetry (CV) curves of graphene- $\text{MnO}_2$  composites reveal no redox peaks due to the surface adsorption/desorption of protons ( $\text{H}^+$ ) or alkaline cations ( $\text{M}^+$ ) on the  $\text{MnO}_2$  surface,<sup>36</sup> indicating that the composites have an ideal capacitive behavior. The main capacitance contributor in the GP/ $\text{MnO}_2$  composite is expected to be the pseudocapacitance provided by  $\text{MnO}_2$ , instead of the double-layer capacitance from GPs. The latter can be proved by the fact that during the CV test increasing the  $\text{MnO}_2$  mass loading from 11.4 wt% to 79.6 wt% results in a much higher current density compared to pristine GPs. We did not study the electrochemical performance of

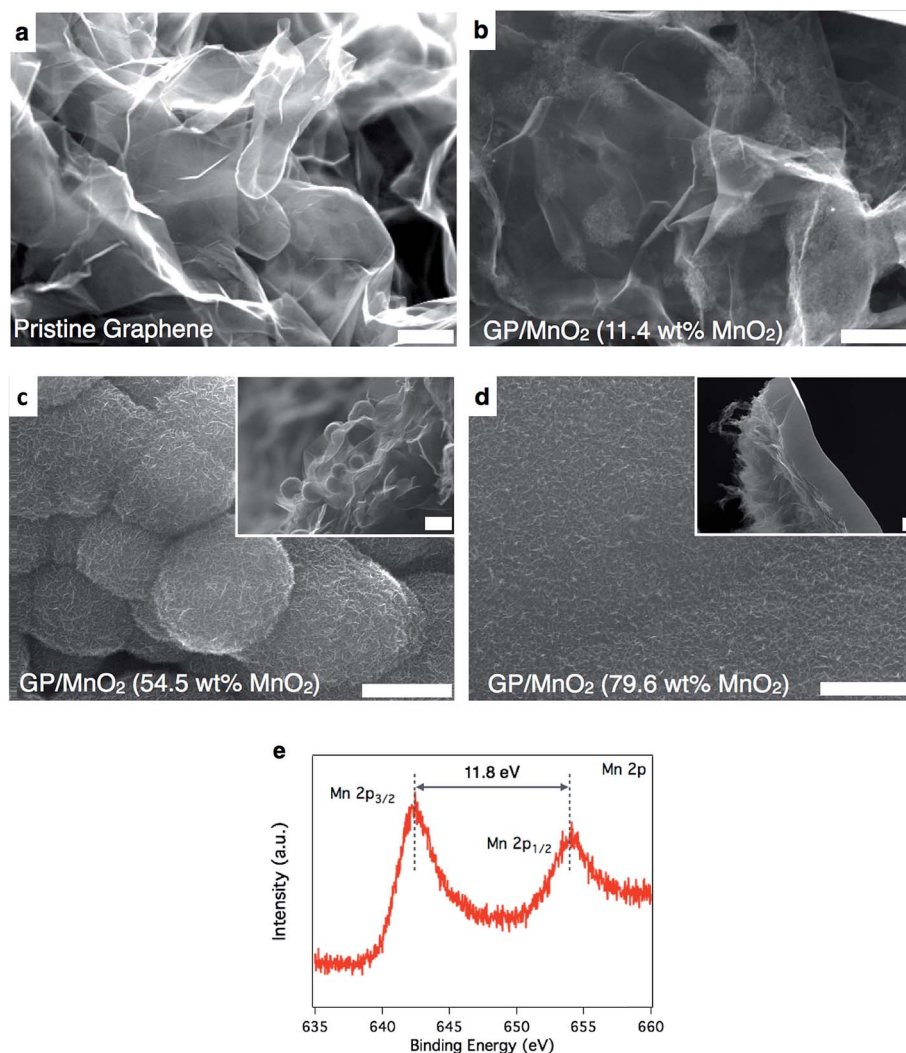


**Fig. 3** (a) SEM image of pristine GPs. (b) SEM image of GP/ $\text{MnO}_2$  (11.4 wt%  $\text{MnO}_2$ ). (c) SEM images of GP/ $\text{MnO}_2$  (54.5 wt%  $\text{MnO}_2$ ). The inset shows the cross-section view of this specimen in which the embedment of  $\text{MnO}_2$  spheres into the surface of GPs is displayed. (d) SEM image of GP/ $\text{MnO}_2$  (79.6 wt%  $\text{MnO}_2$ ). The inset shows the cross-section view of this specimen in which the formation of a thin  $\text{MnO}_2$  layer is observed. All scale bars in the images correspond to 1  $\mu\text{m}$ . (e) Representative Mn 2p XPS spectra of the GP/ $\text{MnO}_2$  composite.

higher  $\text{MnO}_2$  mass loading than 79.6 wt% on the GPs. The rationale for this came from the obtained CV data suggesting a deviation from the most favorable rectangular shape at 79.6 wt%  $\text{MnO}_2$  compared to a lower  $\text{MnO}_2$  content on the GPs. This can be interpreted based on the well-known high resistive behavior of  $\text{MnO}_2$ . The capacitive performance of GP/ $\text{MnO}_2$  composite electrodes was further investigated by the charge-discharge test. For practical applications, both specific capacitance and volumetric capacitance are critical considering the limited space and load under certain circumstances. Fig. 4b

shows the increase of both specific and volumetric capacitance of GP/ $\text{MnO}_2$  composite electrodes due to the increased mass of  $\text{MnO}_2$  as revealed by the SEM images in Fig. 3. The GP/ $\text{MnO}_2$  composite electrode shows specific and volumetric capacitance up to  $395 \text{ F g}^{-1}$  and  $230 \text{ F cm}^{-3}$ , which outperforms many other carbon/ $\text{MnO}_2$  composite electrodes with specific and volumetric capacitance in the order of  $\sim 150 \text{ F g}^{-1}$  and  $\sim 100 \text{ F cm}^{-3}$ , respectively.<sup>37–39</sup> This high value of volumetric capacitance is probably attributed to the more compact structure of GPs compared to other reported porous carbon materials such as

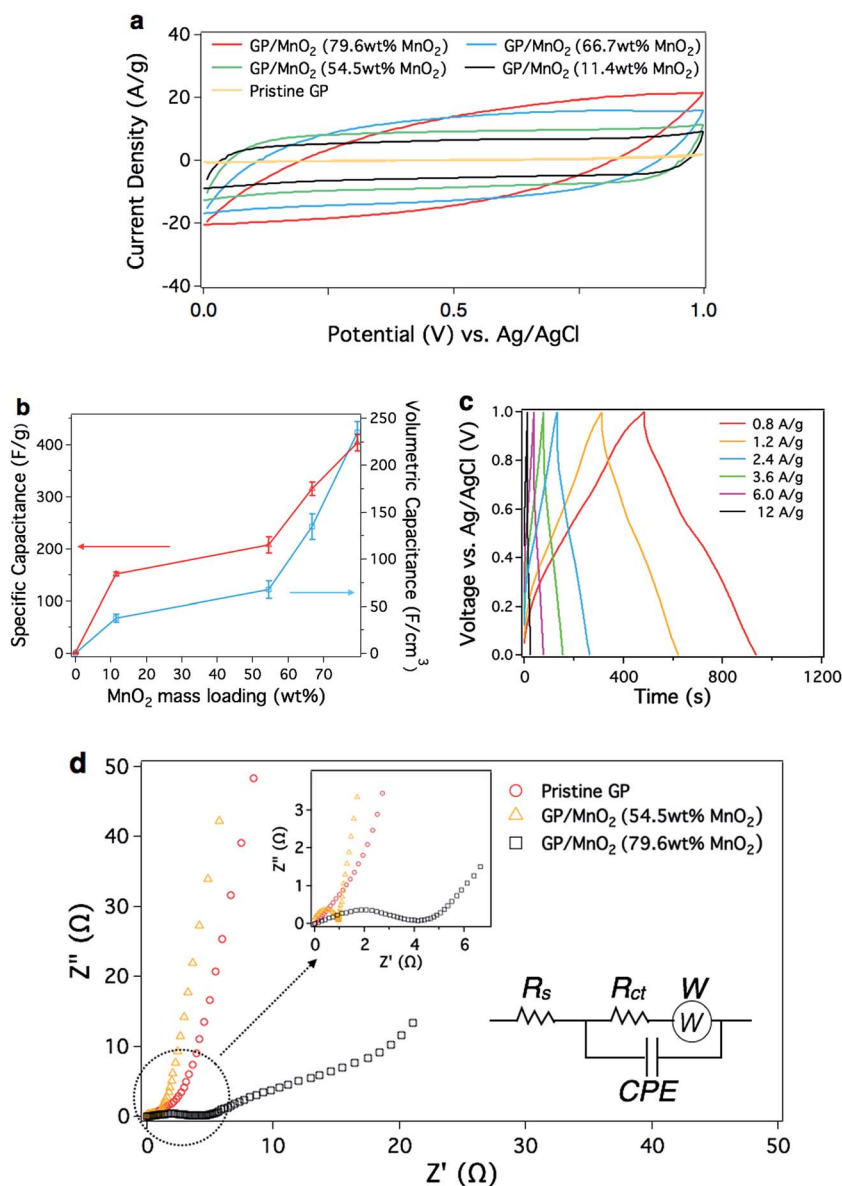


Fig. 4 (a) CV curves measured at  $50 \text{ mV s}^{-1}$  for the pristine GP and GP/ $\text{MnO}_2$  composites with different  $\text{MnO}_2$  mass loadings from 11.4 wt% to 79.6 wt%. (b) Specific capacitance and volumetric capacitance of GPs and GP/ $\text{MnO}_2$  composites as a function of  $\text{MnO}_2$  mass loading. Capacitance was estimated from the galvanostatic charge-discharge test with a current density of  $1 \text{ A g}^{-1}$ . The error bars represent the standard deviations calculated based on 3 tested specimens for each sample. (c) Galvanostatic charge-discharge curves measured at different current densities from 0.8 to  $12 \text{ A g}^{-1}$  for the GP/ $\text{MnO}_2$  composite with 79.6 wt%  $\text{MnO}_2$  mass loading. (d) Nyquist plots for the pristine GP and GP/ $\text{MnO}_2$  composites with different  $\text{MnO}_2$  mass loadings from 54.5 wt% to 79.6 wt%. The inset shows an equivalent series circuit consisting of electrolyte resistance ( $R_s$ ), interface charge transfer resistance ( $R_{ct}$ ), Warburg element ( $W$ ) and constant phase element ( $CPE$ ). All the electrochemical tests were conducted in 1 M aqueous solution of  $\text{Na}_2\text{SO}_4$  using a three-electrode configuration.



GF. Fig. 4c displays the charge–discharge curves of GP/MnO<sub>2</sub> with 79.6 wt% MnO<sub>2</sub> mass loading. From the discharging curve, the specific capacitance of GP/MnO<sub>2</sub> with 79.6 wt% MnO<sub>2</sub> mass loading was calculated to be 395 F g<sup>−1</sup> at 0.8 A g<sup>−1</sup>. These values are higher than those of other reported graphene/MnO<sub>2</sub> materials including the GF/MnO<sub>2</sub> composite (240 F g<sup>−1</sup>, 0.1 A g<sup>−1</sup>),<sup>40</sup> MnO<sub>2</sub>/graphene composite paper (256 F g<sup>−1</sup> at 0.5 A g<sup>−1</sup>),<sup>41</sup> conductive wrapping MnO<sub>2</sub>/graphene composite (380 F g<sup>−1</sup> at 0.1 mA cm<sup>−2</sup>),<sup>32</sup> and 3D graphene/MnO<sub>2</sub> composite (389 F g<sup>−1</sup> at 1 A g<sup>−1</sup>).<sup>12</sup>

The synergy of GPs as a conducting scaffold for MnO<sub>2</sub> in applications as a pseudocapacitive material was further studied by alternating current impedance measurements at a frequency range from 100 kHz to 0.01 Hz. The obtained results are displayed in Fig. 4d in the form of Nyquist plots. The pristine GP shows a negligible charge transfer resistance ( $R_{ct}$ ), which represents the resistance at the interface of the electrode and electrolyte. This result proves the excellent conductivity of GPs at the electrode–electrolyte interface. Based on the equivalent series circuit (Fig. 4d inset),<sup>42,43</sup> the  $R_{ct}$  of the GP/MnO<sub>2</sub> composite electrodes with 54.5 wt% and 79.6 wt% MnO<sub>2</sub> mass loading was calculated. The obtained values were 1.1  $\Omega$  and 3.78  $\Omega$ , respectively. There is a clear trend showing that the increase of MnO<sub>2</sub> mass loading from 54.5 wt% to 79.6 wt% results in the

increase of  $R_{ct}$ , due to the poor electrical conductivity of MnO<sub>2</sub>. Still, the  $R_{ct}$  values of GP/MnO<sub>2</sub> composite electrodes are relatively small compared to other reported graphene/MnO<sub>2</sub> composite electrodes,<sup>28,32</sup> which supports our assumption that GPs can work effectively as a good conducting scaffold in combination with low electrically conductive pseudocapacitive materials such as MnO<sub>2</sub>. In the low frequency region, the slope of the curve represents the electrolyte and proton diffusion resistance. The pristine GP shows the most ideal straight line along the imaginary axis. A typical Warburg capacitive behavior was observed in which the curve slope decreases with increasing the mass loading of MnO<sub>2</sub>, thus indicating higher resistance for ion/proton diffusion.

We also investigated the electrochemical performance of GPs in a redox additive electrolyte system that has been studied intensively in recent years due to its ease of preparation and the potential to yield high energy density.<sup>44–46</sup> We believe that the excellent electrical properties of GPs can greatly facilitate the chemical reaction of redox additives. Fig. 5a shows the CV curves of the pristine GP in 1 M H<sub>2</sub>SO<sub>4</sub> and 30% acetic acid electrolyte with 50 mM hydroquinone (HQ) and 50 mM benzoquinone (BQ) as redox additives. A high current density in the potential range of 0–1.0 V and a couple of redox peaks (HQ to BQ and BQ to HQ) were observed. The charge–discharge curves in

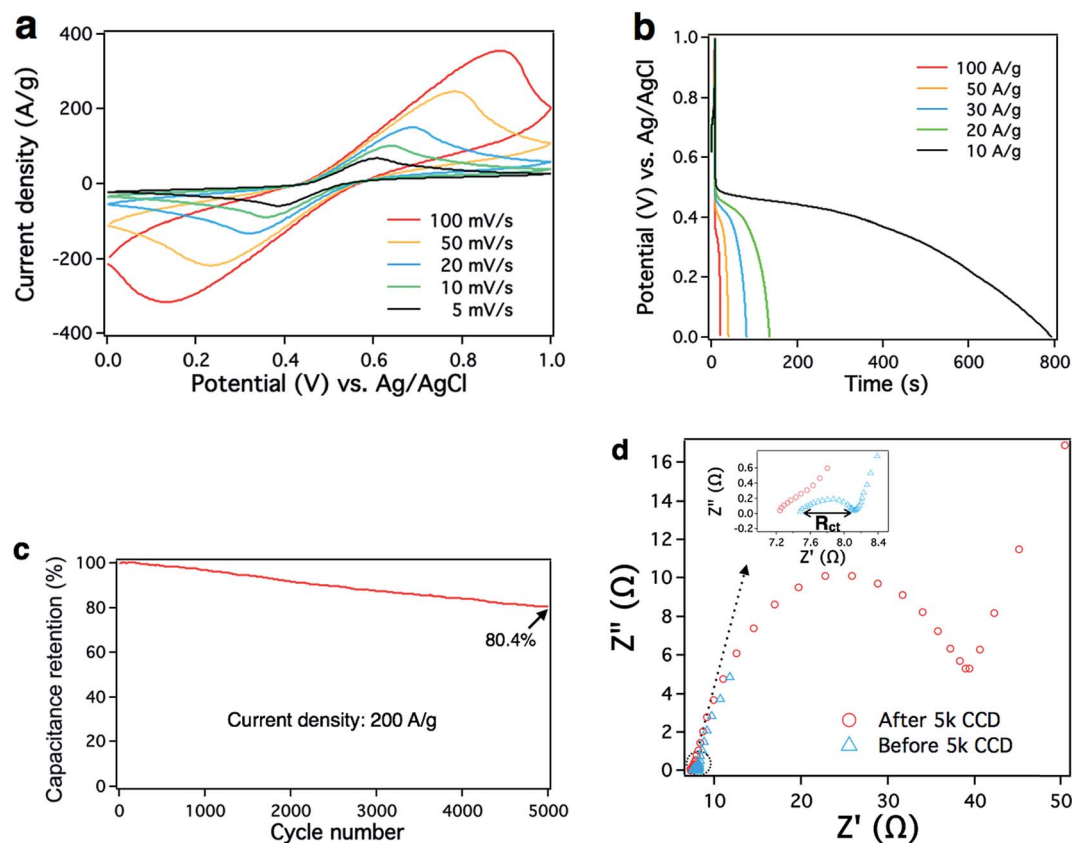
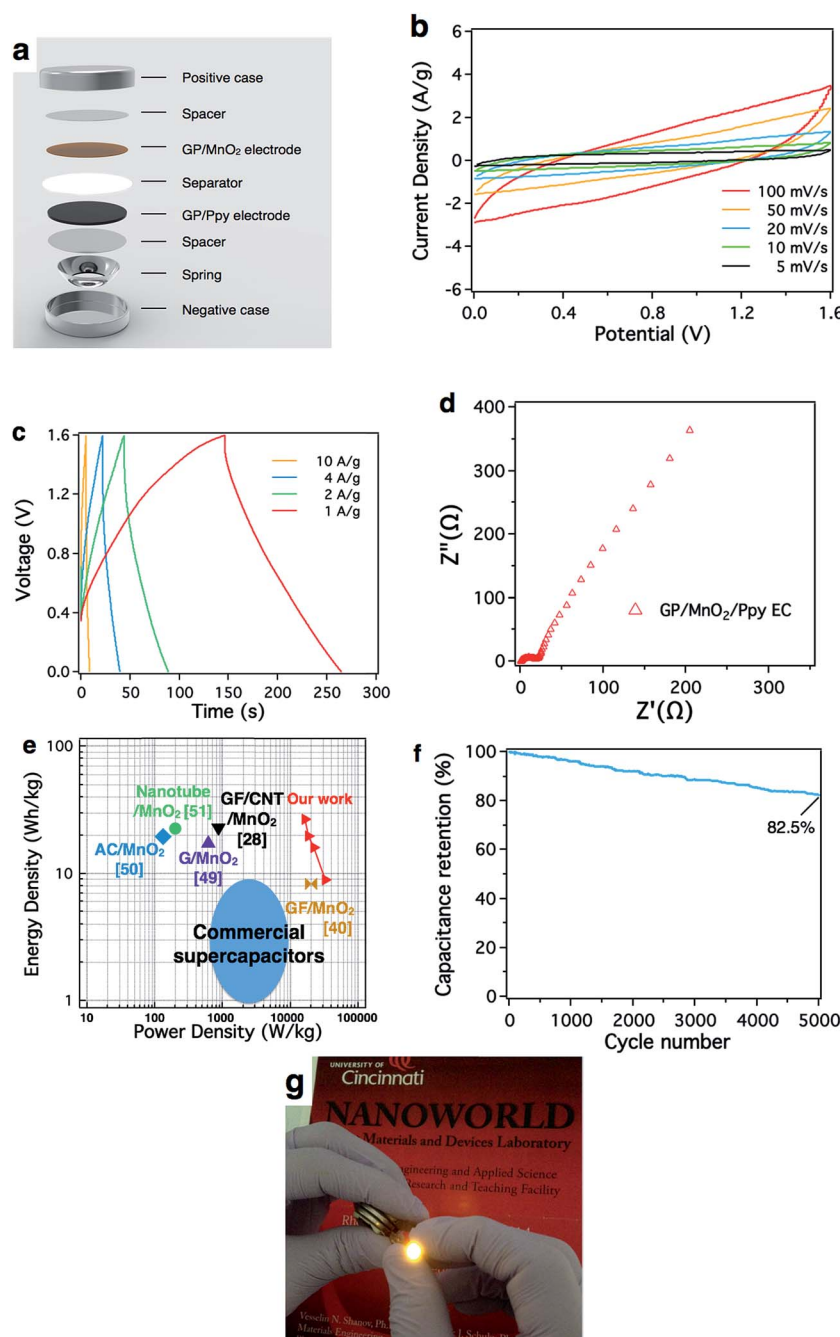


Fig. 5 Electrochemical performance of the pristine GP in 50 mM 1 M H<sub>2</sub>SO<sub>4</sub> and 30% acetic acid as the electrolyte with 50 mM HQ and 50 mM BQ as redox additives. (a) CV curves of GPs in HQBQ at different scan rates. (b) Charge–discharge curves of GPs in HQBQ at different current densities. (c) Capacitance retention curve of GPs in HQBQ after 5k CCD. (d) Comparison of GP impedance in the HQBQ system before and after 5k CCD.

Fig. 5b exhibit an ultrahigh specific capacitance ( $7813 \text{ F g}^{-1}$ ) of GPs at a high current density ( $10 \text{ A g}^{-1}$ ) in the HQBQ electrolyte system, which suggests a good synergy of GPs with the redox additive electrolyte system. This ultrahigh specific capacitance comes from the redox reaction between HQ and BQ,<sup>45</sup> and GPs is proved to efficiently facilitate this process by working as

a lightweight and conductive scaffold rather than a capacitive material. Interestingly, when the discharge current density was reduced from  $20 \text{ A g}^{-1}$  to  $10 \text{ A g}^{-1}$ , a dramatic increase of specific capacitance was observed. Further decrease of the discharge rate down to  $5 \text{ A g}^{-1}$  will lead to an undesirably long discharging time. This might be attributed to the sufficient



**Fig. 6** (a) Illustration of the GP/MnO<sub>2</sub>/Ppy EC assembly. (b) CV curves of GP/MnO<sub>2</sub>/Ppy EC at different scan rates from  $5 \text{ mV s}^{-1}$  to  $100 \text{ mV s}^{-1}$ . (c) Galvanostatic charge–discharge curves measured at different current densities from  $1 \text{ A g}^{-1}$  to  $10 \text{ A g}^{-1}$  for GP/MnO<sub>2</sub>/Ppy EC. (d) Nyquist plots for GP/MnO<sub>2</sub>/Ppy EC from  $100 \text{ kHz}$  to  $0.01 \text{ Hz}$ . (e) Ragone plot showing data from our GP/MnO<sub>2</sub>/Ppy EC compared to reference data from other devices that are based on carbon materials performing in aqueous electrolytes (AC-activated carbon, GF-graphene foam, G-graphene). (f) CCD test of GP/MnO<sub>2</sub>/Ppy EC at a constant current density of  $10 \text{ A g}^{-1}$  conducted over 5000 cycles. (g) A two stacked GP/MnO<sub>2</sub>/Ppy EC fabricated based on this work powering an LED ( $3.0 \text{ V}$ ,  $30 \text{ mA}$ ). All the electrochemical tests were conducted in a coin cell device with GP/MnO<sub>2</sub> as the positive electrode and GP/Ppy as the negative electrode separated by an electrolyte ( $1 \text{ M}$  aqueous solution of  $\text{Na}_2\text{SO}_4$ ) soaked separator.

diffusion of the redox couples into the GPs at a relatively low current density and needs further studies. After 5000 cycles of charge–discharge at a very high current density of  $200 \text{ A g}^{-1}$ , the specific capacitance dropped by 19.6% (Fig. 5c) with an increase of  $R_{\text{ct}}$  after cyclic charge–discharge (CCD) (Fig. 5d). One plausible reason for the increased  $R_{\text{ct}}$  is the agglomeration of BQ in the porous graphene structure considering the low solubility of BQ in water.<sup>45</sup>

The full cell performance of asymmetric ECs made of GP/pseudocapacitive materials was also studied. Since the GP/ $\text{MnO}_2$  electrode shows good capacitive performance in the potential range from 0 to 1.0 V, polypyrrole (Ppy) coated GPs was employed as a negative electrode to expand the potential range of the asymmetric ECs. This is because Ppy has been proven to exhibit good capacitive performance in the working potential range from  $-0.6$  to  $0.2 \text{ V}$ .<sup>28,47,48</sup> It is also important to balance the charge of the positive and negative electrodes in order to maximize the energy density of ECs. In our work, the electrochemical performance of the GP/Ppy electrode was also investigated (Fig. S3†). A successful coverage of GPs by Ppy was proved by SEM images and Raman spectra displayed in Fig. S3.† Further, the GP/Ppy electrode shows a specific capacitance of  $247 \text{ F g}^{-1}$  at  $1 \text{ A g}^{-1}$  (Fig. S3c†). The obtained results allowed balancing the mass ratio of the positive electrode (GP/ $\text{MnO}_2$ ) and the negative electrode (GP/Ppy) to 1 : 2 in order to achieve the maximal energy density of ECs. The assembled EC in this work is represented as GP/ $\text{MnO}_2$ /Ppy EC. In this system  $\text{MnO}_2$  stores energy by adsorption/desorption of protons ( $\text{H}^+$ ) or alkaline cations ( $\text{Na}^+$  in our case) on the oxide surface, while Ppy stores energy by doping/de-doping of anions ( $\text{SO}_4^{2-}$  in our case). In both cases graphene works as a conductive support for those two materials.

Fig. 6a illustrates a schematic structure of the assembled ECs composed of an electrolyte ( $1 \text{ M Na}_2\text{SO}_4$ )-soaked separator sandwiched between positive and negative electrodes. The asymmetric EC shows a typical capacitive behavior in the potential range from 0 to 1.6 V as displayed in Fig. 6b. Slow scan rates cause more pronounced rectangular shapes than high scan rates. This suggests a more resistive behavior of the device at higher scan rates. No redox peaks are observed in Fig. 6b, which is in good agreement with another reported study.<sup>28</sup> The charge–discharge curves of GP/ $\text{MnO}_2$ /Ppy EC under different current densities are displayed in Fig. 6c. Based on the IR drop of the charge–discharge curves, GP/ $\text{MnO}_2$ /Ppy EC exhibits small internal resistances of  $24.5 \text{ } \Omega$ ,  $36.3 \text{ } \Omega$ ,  $44.0 \text{ } \Omega$  and  $48.7 \text{ } \Omega$  at current densities of  $10 \text{ A g}^{-1}$ ,  $4 \text{ A g}^{-1}$ ,  $2 \text{ A g}^{-1}$  and  $1 \text{ A g}^{-1}$ , respectively. The value of the obtained internal resistance is not as low as we expected considering the good electrical conductivity of GPs. A possible explanation is that after the assembly of two different electrodes into a device, the resistance increases because of the differences in the storage mechanisms of these two electrodes. In particular,  $\text{MnO}_2$  stores energy based on the adsorption/desorption of protons ( $\text{H}^+$ ) or *via* alkaline cations ( $\text{M}^+$ ) on the oxide surface, while Ppy stores energy by doping and de-doping of anions. The different mechanisms result in different charge–discharge speeds that contribute to the increased internal resistance of the device. The Nyquist plot in

Fig. 6d reveals  $0.8 \text{ } \Omega$  electrolyte resistance ( $R_s$ ) and  $24.8 \text{ } \Omega$  charge transfer resistance  $R_{\text{ct}}$ , calculated as per ref. 42, suggesting a fast charge transfer between the electrolyte and electrodes. We further calculated the energy density and power density of GP/ $\text{MnO}_2$ /Ppy EC based on the charge–discharge curves in Fig. 6c. The obtained results are presented as a Ragone plot in Fig. 6e. The GP/ $\text{MnO}_2$ /Ppy EC in our work shows a maximum energy density of  $26.7 \text{ W h kg}^{-1}$  at a power density of  $798 \text{ W kg}^{-1}$ , and a maximum power density ( $P_m$ ) of  $16.4 \text{ kW kg}^{-1}$ . The highest  $P_m$  was found to be  $32.7 \text{ kW kg}^{-1}$  with an energy density of  $8.9 \text{ W h kg}^{-1}$  at a power density of  $8.0 \text{ kW kg}^{-1}$ . Such performance is superior compared to other ECs reported in the literature,<sup>28,49–51</sup> especially with regard to a similar GF/ $\text{MnO}_2$  device showing a lower energy density of  $8.3 \text{ W h kg}^{-1}$  at a power density of  $20 \text{ kW kg}^{-1}$  respectively.<sup>40</sup> The GP/ $\text{MnO}_2$ /Ppy EC also exhibits a good cycle life with 85% capacitance retention after 5000 cycles of charge–discharge at  $10 \text{ A g}^{-1}$  (Fig. 6f). Furthermore, two stacked GP/ $\text{MnO}_2$ /Ppy ECs were able to power a LED ( $3.0 \text{ V}$ ,  $30 \text{ mA}$ ) for 1.5 min as shown in Fig. 6g.

## 4. Conclusions

We reported a new design and fabrication process of an electrode material called graphene pellets (GPs) for energy storage applications. The employed catalyst in the form of a sintered nickel template can be easily converted into a GP by CVD. The GPs exhibit good electrical conductivity, electromechanical stability and morphology with a mesoporous structure thus providing great potential for energy storage applications. GP/ $\text{MnO}_2$  composites prepared by the described simple electrochemical deposition of  $\text{MnO}_2$  onto the GP surface showed both high specific and volumetric capacitance with small charge-transfer resistance. This demonstrates good synergy between GPs and  $\text{MnO}_2$ . The excellent electrical and mechanical properties of GPs also show great potential in facilitating chemical reactions typical for redox additive electrolyte systems. Moreover, when the GP/ $\text{MnO}_2$  electrode was assembled with the GP/polypyrrole electrode, the obtained full coin cell showed good performance. The simplicity of the 3D graphene preparation allows GPs to compete with or replace GF in many energy storage applications.

## Acknowledgements

The authors acknowledge the financial support from the UC Office of Research and the Mathewson Renewable Energy Research Fund. The authors appreciate the SSA and pore size measurement of the GPs conducted by Dr Paul Kester from Micromeritics Instrument Corporation.

## References

- 1 Z. Chen, W. Ren, L. Gao, B. Liu, S. Pei and H.-M. Cheng, *Nat. Mater.*, 2011, **10**, 424–428.
- 2 X. Yu, B. Lu and Z. Xu, *Adv. Mater.*, 2014, **26**, 1044–1051.

- 3 X.-C. Dong, H. Xu, X.-W. Wang, Y.-X. Huang, M. B. Chan-Park, H. Zhang, L.-H. Wang, W. Huang and P. Chen, *ACS Nano*, 2012, **6**, 3206–3213.
- 4 Y. He, W. Chen, X. Li, Z. Zhang, J. Fu, C. Zhao and E. Xie, *ACS Nano*, 2013, **7**, 174–182.
- 5 X. Dong, X. Wang, J. Wang, H. Song, X. Li, L. Wang, M. B. Chan-Park, C. M. Li and P. Chen, *Carbon*, 2012, **50**, 4865–4870.
- 6 C. Zhao, W. Zheng, X. Wang, H. Zhang, X. Cui and H. Wang, *Sci. Rep.*, 2013, **3**, 2986.
- 7 X. Cao, Y. Shi, W. Shi, G. Lu, X. Huang, Q. Yan, Q. Zhang and H. Zhang, *Small*, 2011, **7**, 3163–3168.
- 8 J. Luo, J. Liu, Z. Zeng, C. F. Ng, L. Ma, H. Zhang, J. Lin, Z. Shen and H. J. Fan, *Nano Lett.*, 2013, **13**, 6136–6143.
- 9 N. Li, Z. Chen, W. Ren, F. Li and H.-M. Cheng, *Proc. Natl. Acad. Sci. U. S. A.*, 2012, **109**, 17360–17365.
- 10 G. Zhou, L. Li, C. Ma, S. Wang, Y. Shi, N. Koratkar, W. Ren, F. Li and H.-M. Cheng, *Nano Energy*, 2015, **11**, 356–365.
- 11 W. Zhang, J. Zhu, H. Ang, Y. Zeng, N. Xiao, Y. Gao, W. Liu, H. H. Hng and Q. Yan, *Nanoscale*, 2013, **5**, 9651–9658.
- 12 B. G. Choi, M. Yang, W. H. Hong, J. W. Choi and Y. S. Huh, *ACS Nano*, 2012, **6**, 4020–4028.
- 13 S. Chen, J. Zhu, X. Wu, Q. Han and X. Wang, *ACS Nano*, 2010, **4**, 2822–2830.
- 14 K. Zhang, L. Mao, L. L. Zhang, H. S. O. Chan, X. S. Zhao and J. Wu, *J. Mater. Chem.*, 2011, **21**, 7302–7307.
- 15 F. Liu, S. Song, D. Xue and H. Zhang, *Adv. Mater.*, 2012, **24**, 1089–1094.
- 16 Z. Wen, X. Wang, S. Mao, Z. Bo, H. Kim, S. Cui, G. Lu, X. Feng and J. Chen, *Adv. Mater.*, 2012, **24**, 5610–5616.
- 17 Y. Xu, K. Sheng, C. Li and G. Shi, *ACS Nano*, 2010, **4**, 4324–4330.
- 18 J. H. Lee, N. Park, B. G. Kim, D. S. Jung, K. Im, J. Hur and J. W. Choi, *ACS Nano*, 2013, **7**, 9366–9374.
- 19 L. Zhang, N. T. Alvarez, M. Zhang, M. Haase, R. Malik, D. Mast and V. Shanov, *Carbon*, 2015, **82**, 353–359.
- 20 W. Li, S. Gao, L. Wu, S. Qiu, Y. Guo, X. Geng, M. Chen, S. Liao, C. Zhu, Y. Gong, M. Long, J. Xu, X. Wei, M. Sun and L. Liu, *Sci. Rep.*, 2013, **3**, 2125.
- 21 C. Shan, H. Tang, T. Wong, L. He and S.-T. Lee, *Adv. Mater.*, 2012, **24**, 2491–2495.
- 22 Z. Chen, W. Ren, B. Liu, L. Gao, S. Pei, Z.-S. Wu, J. Zhao and H.-M. Cheng, *Carbon*, 2010, **48**, 3543–3550.
- 23 D. Yu, K. Goh, H. Wang, L. Wei, W. Jiang, Q. Zhang, L. Dai and Y. Chen, *Nat. Nanotechnol.*, 2014, **9**, 555–562.
- 24 X. Wang, Y. Zhang, C. Zhi, X. Wang, D. Tang, Y. Xu, Q. Weng, X. Jiang, M. Mitome, D. Golberg and Y. Bando, *Nat. Commun.*, 2013, **4**, 2905.
- 25 K. Jurewicz, E. Frackowiak and F. Béguin, *Appl. Phys. A*, 2004, **78**, 981–987.
- 26 C. Vix-Guterl, E. Frackowiak, K. Jurewicz, M. Friebe, J. Parmentier and F. Béguin, *Carbon*, 2005, **43**, 1293–1302.
- 27 F. Béguin, M. Friebe, K. Jurewicz, C. Vix-Guterl, J. Dentzer and E. Frackowiak, *Carbon*, 2006, **44**, 2392–2398.
- 28 J. Liu, L. Zhang, H. B. Wu, J. Lin, Z. Shen and X. W. Lou, *Energy Environ. Sci.*, 2014, **7**, 3709–3719.
- 29 A. Sumboja, C. Y. Foo, X. Wang and P. S. Lee, *Adv. Mater.*, 2013, **25**, 2809–2815.
- 30 J. A. Rogers, T. Someya and Y. Huang, *Science*, 2010, **327**, 1603–1607.
- 31 K. S. Kim, Y. Zhao, H. Jang, S. Y. Lee, J. M. Kim, K. S. Kim, J.-H. Ahn, P. Kim, J.-Y. Choi and B. H. Hong, *Nature*, 2009, **457**, 706–710.
- 32 G. Yu, L. Hu, N. Liu, H. Wang, M. Vosgueritchian, Y. Yang, Y. Cui and Z. Bao, *Nano Lett.*, 2011, **11**, 4438–4442.
- 33 S. W. Lee, J. Kim, S. Chen, P. T. Hammond and Y. Shao-Horn, *ACS Nano*, 2010, **4**, 3889–3896.
- 34 M. Toupin, T. Brousse and D. Bélanger, *Chem. Mater.*, 2004, **16**, 3184–3190.
- 35 A. L. M. Reddy, M. M. Shaijumon, S. R. Gowda and P. M. Ajayan, *Nano Lett.*, 2009, **9**, 1002–1006.
- 36 Q. Qu, P. Zhang, B. Wang, Y. Chen, S. Tian, Y. Wu and R. Holze, *J. Phys. Chem. C*, 2009, **113**, 14020–14027.
- 37 J. R. Miller and A. F. Burke, *Electrochem. Soc. Interface*, 2008, **17**, 53.
- 38 P. Simon and A. F. Burke, *Electrochem. Soc. Interface*, 2008, **17**, 38.
- 39 Y. J. Kim, Y. Abe, T. Yanagiura, K. C. Park, M. Shimizu, T. Iwazaki, S. Nakagawa, M. Endo and M. S. Dresselhaus, *Carbon*, 2007, **45**, 2116–2125.
- 40 A. Bello, O. O. Fashedemi, J. N. Lekitima, M. Fabiane, D. Dodoo-Arhin, K. I. Ozoemena, Y. Gogotsi, A. T. Charlie Johnson and N. Manyala, *AIP Adv.*, 2013, **3**, 082118.
- 41 Z. Li, Y. Mi, X. Liu, S. Liu, S. Yang and J. Wang, *J. Mater. Chem.*, 2011, **21**, 14706–14711.
- 42 B. G. Choi, J. Hong, W. H. Hong, P. T. Hammond and H. Park, *ACS Nano*, 2011, **5**, 7205–7213.
- 43 M. V. Reddy, T. Yu, C. H. Sow, Z. X. Shen, C. T. Lim, G. V. Subba Rao and B. V. R. Chowdari, *Adv. Funct. Mater.*, 2007, **17**, 2792–2799.
- 44 G. Ma, M. Dong, K. Sun, E. Feng, H. Peng and Z. Lei, *J. Mater. Chem. A*, 2015, **3**, 4035–4041.
- 45 D. Vonlanthen, P. Lazarev, K. A. See, F. Wudl and A. J. Heeger, *Adv. Mater.*, 2014, **26**, 5095–5100.
- 46 S.-E. Chun, B. Evanko, X. Wang, D. Vonlanthen, X. Ji, G. D. Stucky and S. W. Boettcher, *Nat. Commun.*, 2015, **6**, 7818.
- 47 C. Xu, J. Sun and L. Gao, *J. Mater. Chem.*, 2011, **21**, 11253–11258.
- 48 Y. Zhao, J. Liu, Y. Hu, H. Cheng, C. Hu, C. Jiang, L. Jiang, A. Cao and L. Qu, *Adv. Mater.*, 2013, **25**, 591–595.
- 49 T. Cottineau, M. Toupin, T. Delahaye, T. Brousse and D. Bélanger, *Appl. Phys. A*, 2006, **82**, 599–606.
- 50 Q. T. Qu, Y. Shi, S. Tian, Y. H. Chen, Y. P. Wu and R. Holze, *J. Power Sources*, 2009, **194**, 1222–1225.
- 51 M. Huang, Y. Zhang, F. Li, L. Zhang, R. S. Ruoff, Z. Wen and Q. Liu, *Sci. Rep.*, 2014, **4**, 3878.